

THE STAR FORMATION RATE INTENSITY DISTRIBUTION FUNCTION—IMPLICATIONS FOR THE COSMIC STAR FORMATION RATE HISTORY OF THE UNIVERSE^{1,2,3,4}

KENNETH M. LANZETTA, NORIAKI YAHATA, SEBASTIAN PASCARELLE
Department of Physics and Astronomy, State University of New York at Stony Brook
Stony Brook, NY 11794–3800, U.S.A.

HSIAO-WEN CHEN
Observatories of the Carnegie Institute of Washington
813 Santa Barbara St., Pasadena, CA, 91101, U.S.A.

and

ALBERTO FERNÁNDEZ-SOTO⁵
Osservatorio Astronomico di Brera
Via Bianchi 46, Merate (LC). I-23807, ITALY

ABSTRACT

We address the effects of cosmological surface brightness dimming on observations of faint galaxies by examining the distribution of “unobscured” star formation rate intensities versus redshift. We use the star formation rate intensity distribution function to assess the ultraviolet luminosity density versus redshift, based on our photometry and photometric redshift measurements of faint galaxies in the HDF and the HDF–S WFPC2 and NICMOS fields. We find

¹Based on observations with the NASA/ESA Hubble Space Telescope, obtained at the Space Telescope Science Institute, which is operated by the Association of Universities for Research in Astronomy, Inc., under NASA contract NAS5–26555.

²Based on observations made at the Kitt Peak National Observatory, National Optical Astronomy Observatories, which is operated by the Association of Universities for Research in Astronomy, Inc. (AURA) under cooperative agreement with the National Science Foundation.

³Based on observations collected at the European Southern Observatory, Paranal, Chile (VLT-UT1 Science Verification Program).

⁴Observations have been carried out using the ESO New Technology Telescope (NTT) at the La Silla observatory under Program-ID Nos. 61.A-9005(A), 162.O-0917, 163.O-0740, 164.O-0561.

⁵Marie Curie Fellow.

that (1) previous measurements have missed a dominant fraction of the ultraviolet luminosity density of the universe at high redshifts by neglecting cosmological surface brightness dimming effects, which are important at redshifts larger than $z \approx 2$, (2) the incidence of the highest intensity star forming regions increases monotonically with redshift, and (3) the ultraviolet luminosity density plausibly increases monotonically with redshift through the highest redshifts observed. By measuring the spectrum of the luminosity density versus redshift, we also find that (4) previous measurements of the ultraviolet luminosity density at redshifts $z < 2$ must be reduced by a factor ≈ 2 to allow for the spectrum of the luminosity density between rest-frame wavelengths 1500 and 2800 Å. And by comparing with observations of high-redshift damped Ly α absorption systems detected toward background QSOs, we further find that (5) the distribution of star formation rate intensities matches the distribution of neutral hydrogen column densities at redshifts $z \approx 2$ through 5, which establishes a quantitative connection between high-redshift galaxies and high column density gas and suggests that high-redshift damped Ly α absorption systems trace lower star formation rate intensity regions of the same galaxies detected in star light in the HDF and HDF–S. Because our measurements neglect the effects of obscuration by dust, they represent *lower limits* to the total star formation rate density.

Subject headings: cosmology: observations; galaxies: evolution

1. INTRODUCTION

The rest-frame ultraviolet luminosity density of the universe traces the history of cosmic star formation because it is produced by hot, massive, young stars. Previous measurements have found that the ultraviolet luminosity density increases with redshift to a maximum at redshift $z \approx 1$ to 2 and then decreases (Madau et al. 1996) or remains constant (Madau, Pozzetti, & Dickinson 1998; Steidel et al. 1999; Hopkins, Connolly, & Szalay 2000) with redshift to higher redshifts. These previous measurements have been interpreted in the context of galaxy formation and evolution scenarios as indicating that the stellar content of galaxies was formed gradually, over most of cosmic time (e.g. Somerville, Primack, & Faber 2001).

But previous measurements have neglected cosmological surface brightness dimming effects, which can play a dominant role in setting what is observed at high redshifts (Pascarelle, Lanzetta, & Fernández-Soto 1998). Specifically, surface brightness (per unit frequency interval) decreases with redshift as $(1+z)^{-3}$ due to the expansion of the universe. This has an

important consequence for observations of distant galaxies: while both intrinsically bright and intrinsically faint regions of low-redshift galaxies are accessible to observation, only intrinsically bright regions of high-redshift galaxies are accessible to observation—intrinsically faint regions of high-redshift galaxies are of low surface brightness and are simply not detected against the background noise. Thus all measurements *miss* some fraction of the light of distant galaxies; this fraction is small for low-redshift galaxies but can be dominant for high-redshift galaxies.

Here we address this issue by examining the distribution of “unobscured” star formation rate intensities versus redshift—i.e. the star formation rate intensities that are directly inferred from the observed rest-frame ultraviolet light that is not obscured by intervening dust. We use the star formation rate intensity distribution function to assess the ultraviolet luminosity density versus redshift, based on our photometry and photometric redshift measurements of faint galaxies in the Hubble Deep Field (HDF) and Hubble Deep Field South (HDF-S) WFPC2 and NICMOS fields (Lanzetta, Yahil, & Fernández-Soto 1996; Fernández-Soto, Lanzetta, & Yahil 1999; Yahata et al. 2000; Yahata et al. 2001 in preparation). The star formation rate intensity distribution function bears on the issue because it makes explicit the effects of cosmological surface brightness dimming on observations of high-redshift galaxies, thereby allowing the amount by which previous measurements have underestimated the ultraviolet luminosity density at high redshifts to be directly estimated. Because our measurements neglect the effects of obscuration by dust, they represent *lower limits* to the total star formation rate density.

The framework of the unobscured star formation rate intensity and the star formation rate intensity distribution function is presented in § 2. The photometry and photometric redshift measurements are summarized in § 3, the angular area versus depth relations are summarized in § 4, and the Stony Brook faint galaxy redshift survey is summarized in § 5. The star formation rate intensity distribution function measurements are described in § 6, results are described in § 7, and the connection with the neutral hydrogen column density distribution function is described in § 8. The summary and conclusions are presented in § 9. Unless otherwise stated, we adopt a standard Friedmann cosmological model of dimensionless Hubble constant $h_{100} = H_0/(100 \text{ km s}^{-1} \text{ Mpc}^{-3})$ and deceleration parameter $q_0 = 0.5$; this is the same cosmological model adopted for previous measurements of the rest-frame ultraviolet luminosity density.

2. FRAMEWORK

To address the issue of the effects of cosmological surface brightness dimming, we examine the distribution of “unobscured” star formation rate intensities versus redshift. We designate the unobscured star formation rate intensity as x and the star formation rate intensity distribution function as $h(x)$. The star formation rate intensity distribution function $h(x)$ bears on the issue because it makes explicit the effects of cosmological surface brightness dimming on observations of high-redshift galaxies.

By “unobscured star formation rate intensity,” we mean the star formation rate intensity that is *directly inferred* from the rest-frame ultraviolet light that is not obscured by intervening dust. Hence unobscured star formation rate intensity (measured, say, in units of $M_{\odot} \text{ yr}^{-1} \text{ kpc}^{-2}$) is *equivalent to* rest-frame ultraviolet luminosity per unit area (measured, say, in units of $\text{erg s}^{-1} \text{ Hz}^{-1} \text{ kpc}^{-2}$), once some fixed scaling between ultraviolet luminosity and star formation rate (which is set by the stellar initial mass function) is specified. To determine the *total* star formation rate intensity from the unobscured star formation rate intensity would require knowledge of the effects of obscuration by intervening dust, which is beyond the scope of the present analysis. Rather, here we address *only* the effects of cosmological surface brightness dimming. We emphasize that because our measurements neglect the effects of obscuration by dust, they represent *lower limits* to the total star formation rate density.

We define the star formation rate intensity distribution function $h(x)$ in such a way that $h(x)dx$ is the projected proper area per comoving volume of unobscured star formation rate intensity in the interval x to $x + dx$. The star formation rate intensity distribution function $h(x)$ is a fundamental statistical description of the evolving galaxy population, similar in spirit to the galaxy luminosity function but cast in terms of star formation rate intensity (derived from measurement of surface brightness) rather than luminosity (derived from measurement of energy flux). For our purposes, the first moment of $h(x)$

$$\int_0^{\infty} x h(x) dx \tag{1}$$

is of particular interest. The first moment of $h(x)$ is the unobscured star formation rate density $\dot{\rho}_S$, which is equivalent to within a factor of scale to the ultraviolet luminosity density ρ_{ν} . Equation (1) makes explicit the effects of cosmological surface brightness dimming on measurement of the ultraviolet luminosity density: In equation (1), the limits of integration extend from $x = 0$ through ∞ . But in practice, a given observation (at a given redshift) is sensitive only to some star formation rate intensity threshold x_{\min} , which is set by the surface brightness threshold of the observation (and the redshift). Whether or not a given observation (at a given redshift) is suitable for measuring the ultraviolet luminosity density

depends on whether or not x_{\min} is less than the value of x above which the bulk of the ultraviolet luminosity density is emitted. Here we assess the ultraviolet luminosity density versus redshift and determine the amount by which previous measurements have underestimated the ultraviolet luminosity density at high redshifts, based on our photometry and photometric redshift measurements of faint galaxies in the HDF and HDF–S WFPC2 and NICMOS fields.

3. PHOTOMETRY AND PHOTOMETRIC REDSHIFT MEASUREMENTS

3.1. Photometry

Details of our photometry of faint galaxies in the HDF and HDF–S WFPC2 and NICMOS fields have been described previously by Fernández-Soto et al. (1999) and Yahata et al. (2000). In this section, we summarize important aspects of our photometry techniques.

We processed all available space- and ground-based optical- and infrared-wavelength images of the HDF and HDF–S WFPC2 and NICMOS fields. These images include discretionary, GO, and GTO observations obtained with the Hubble Space Telescope (HST) and images obtained with the Kitt Peak National Observatory (KPNO) 4 m telescope and the European Southern Observatory (ESO) New Technology Telescope (NTT) and Very Large Telescope UT–1 (VLT UT–1). We registered the images (to an accuracy of typically 0.25 pixel for space-based images and 0.5 pixel for ground-based images) by appropriate translation, rotation, and scaling using our own algorithms and software, and we identified and masked cosmic ray events using our own algorithms and software. Details of the observations are summarized in Table 1.

We detected objects in the images at multiple bandpasses using the SExtractor program (Bertin & Arnouts 1996), starting at shorter wavelengths and working toward longer wavelengths. First, we detected objects in the images of a fiducial bandpass (typically the F814W bandpass). Then, we masked regions around detected objects and detected objects in the unmasked regions of images of a longer-wavelength bandpass (typically the F160W or H bandpass). Finally, we repeated these steps for remaining images of longer-wavelength bandpasses (typically the F222M or K bandpass). In this way, the shorter-wavelength bandpasses (which are generally of higher sensitivity and resolution but which are unsuitable for detecting high-redshift galaxies) were used to detect low- and moderate-redshift galaxies and the longer-wavelength bandpasses (which are generally of lower sensitivity and resolution but which are suitable for detecting high-redshift galaxies) were used to detect high-redshift galaxies. Details of the object detection are summarized in Table 2.

We performed photometry using our quasi-optimal photometry technique, which fits model spatial profiles of the detected objects to the space- and ground-based images (Yahata et al. 2000). We determined model spatial profiles by using non-negative least squares image reconstruction (Puetter & Yahil 1999) of one or more of the space-based images. The quasi-optimal photometry technique offers three important advantages in comparison with conventional methods: (1) it provides higher signal-to-noise ratio measurements, (2) it accounts for point-spread function variations between the images, and (3) it accounts for uncertainty correlations between nearby, overlapping neighbors.

3.2. Photometric Redshift Measurements

Details of our photometric redshift measurements of faint galaxies in the HDF and HDF–S WFPC2 and NICMOS fields have been described previously by Lanzetta et al. (1996), Fernández-Soto et al. (1999), and Yahata et al. (2000). In this section, we summarize important aspects of our photometric redshift measurement techniques.

We measured photometric redshifts (and spectral types) of galaxies using our redshift likelihood technique (Lanzetta et al. 1996; Fernández-Soto et al. 1999) with a sequence of six spectrophotometric templates, including templates of E/S0, Sbc, Scd, and Irr galaxies and low- and high-extinction starburst galaxies (which we designate as SB1 and SB2), and incorporating the effects of intrinsic and intervening absorption by neutral hydrogen.

We assessed the accuracy and reliability of the photometric redshift measurements by comparing photometric redshift measurements with spectroscopic redshift measurements of galaxies identified in the HDF and HDF–S. Results indicate that at all redshifts $z < 6$ that have yet been examined, the photometric redshift measurements are characterized by an RMS relative dispersion with respect to the spectroscopic redshift measurements of $\Delta z / (1 + z) \lesssim 0.065$ and that there are no known examples of photometric redshift measurements that differ from spectroscopic redshift measurements by more than a few times the RMS relative dispersion (Yahata et al. 2000; Fernández-Soto et al. 2001). These results set an upper limit to the *systematic* uncertainty of the photometric redshift technique, to which must be added, of course, the uncertainty due to effects of photometric error to determine the total uncertainty of a particular measurement.

4. ANGULAR AREA VERSUS DEPTH RELATION

The angular area versus depth relations set the angular area accessible to the observations as a function of “depth,” where “depth” might in general be any one of a number of observed or intrinsic properties of galaxies (e.g., energy flux in a given observed-frame bandpass, luminosity at a given rest-frame wavelength, or surface brightness at a given rest-frame wavelength). For the purpose of the present analysis, we take “depth” to be unobscured star formation rate intensity x . The angular area versus depth relation must account for several important effects: First, the sensitivities of the individual images (especially the NICMOS images) vary with position. Second, objects are detected in one or more observed-frame bandpasses, whereas results are determined with respect to a single observed-frame bandpass or rest-frame wavelength. Finally, object detection is performed at multiple bandpasses, which introduces complicated conditional selection criteria into the analysis.

We determined the angular area versus depth relation as a function of redshift z and unobscured star formation rate intensity x using surface brightness sensitivity maps of the individual HDF and HDF-S WFPC2 and NICMOS images. First, we determined the surface brightness sensitivity maps by scaling the sky variance maps in such a way as to match the faint envelopes of surface brightnesses actually included into the segmentation maps of the galaxies. (This assumes that the sky variance maps trace the shape but not the normalization of the surface brightness sensitivity maps.) Then, we calculated the surface brightness expected for given values of z and x , using the K correction of an Irr galaxy. (No cosmological model is required, because the dependence of surface brightness on redshift is independent of cosmological model.) Then, we summed the angular areas of the pixels that are sensitive enough to detect the surface brightness expected for the given values of z and x , which we identified by examining the surface brightness sensitivity maps of the images used for object detection. Finally, we repeated these steps for a range of values of z and x .

The angular area versus depth relation $\Omega(z, x)$ as a function of redshift z and star formation rate intensity x is shown in Figure 1. In Figure 1, white regions represent $\Omega(z, x) = 0$, black regions represent $\Omega(z, x) = 11.7 \text{ arcmin}^2$ (i.e. the total angular area spanned by the observations), and grey regions represent intermediate values of $\Omega(z, x)$.

5. STONY BROOK FAINT GALAXY REDSHIFT SURVEY

Our catalogs of photometry and photometric redshift measurements include nearly 5000 faint galaxies, of which nearly 1000 yield redshift measurements $z > 2$ and more than 50 yield redshift measurements $z > 5$ (ranging up to and beyond $z = 10$). The catalogs of photometry

and photometric redshift measurements and the angular area versus depth relations together constitute a galaxy redshift survey to the faintest limits and highest redshifts yet accessible, which we designate as the Stony Brook faint galaxy redshift survey.

Properties of the survey are summarized in Figure 2, which shows the redshift measurement distributions of all galaxies identified in the HDF and HDF–S WFPC2 and NICMOS fields. The redshift measurement distributions of galaxies identified in the HDF and HDF–S WFPC2 field are characterized by broad peaks at redshift $z \approx 1$ and tails extending to redshifts $z > 5$. (The distributions are statistically different from one another, with the HDF–S WFPC2 field exhibiting a statistically significant excess of galaxies of redshift $z > 2$ compared with the HDF, and both distributions exhibit statistically significant large-scale fluctuations. Because the HDF–S fields were chosen due to their proximity to a known QSO of redshift $z = 2.2$, the HDF–S field may be biased toward galaxies of redshift $z \approx 2$.) The redshift measurement distribution of galaxies identified in the HDF–S NICMOS field is characterized by a broad peak at redshift $z \approx 1$ and a tail extending to redshifts $z > 10$.

We note several points about the nature of the galaxies of redshift measurement $z > 6$ identified in our survey. First, our photometric redshift measurements have been directly compared with spectroscopic redshift measurements at redshifts $z \lesssim 6$ but have not been directly compared with spectroscopic redshift measurements at redshifts $z \gtrsim 6$. (See Fernández-Soto et al. 2001 for the latest description of this comparison and for an assessment of the accuracy and reliability of the photometric and spectroscopic redshift measurement techniques.) Second, the redshift likelihood functions of most (but not all) of the galaxies of redshift measurement $z > 6$ are sufficiently broad or multiply-peaked that lower-redshift solutions cannot be excluded. Hence a “best-fit” redshift measurement $z > 6$ does not by itself indicate a redshift $z > 6$ —in every case the redshift likelihood function must be consulted to identify the range of allowed redshifts. And third, our bootstrap error analysis (described below) explicitly accounts for cases of broad or multiply-peaked redshift likelihood functions. The emphasis of the present analysis is on redshifts $z < 6$, and the galaxies of redshift measurement $z > 6$ do not bear significantly on our primary conclusions.

6. STAR FORMATION RATE INTENSITY DISTRIBUTION FUNCTION MEASUREMENTS

The objective of the analysis is to determine the star formation rate intensity distribution function by considering all pixels in all galaxies in all fields on an individual pixel-by-pixel basis. In this section, we describe our measurements of the star formation rate intensity distribution function.

First, we determined the rest-frame 1500 Å luminosity of each pixel, using the measured energy flux of the pixel, the redshift of the pixel (which is set by the redshift of the host galaxy), the empirical K correction of the pixel (which is set by the spectrophotometric template of the host galaxy), and the cosmological model. Then, we determined the star formation rate of each pixel, using a Salpeter stellar initial mass function to scale rest-frame 1500 Å luminosity to star formation rate. Then, we determined the proper area of each pixel, using the redshift of the pixel, the angular plate scale of the image, and the cosmological model. Then, we divided the star formation rate by the proper area of each pixel to determine the star formation rate intensity x of the pixel. The star formation rate intensity x is measured, say, in units of $M_{\odot} \text{ yr}^{-1} \text{ kpc}^{-2}$.

Next, we summed the proper areas of all pixels within given star formation rate intensity and redshift intervals. Then, we determined the comoving volumes that correspond to the redshift intervals, using the angular area versus depth relation and the cosmological model. Then, we divided the summed proper areas by the appropriate star formation rate intensity intervals and comoving volumes to determine the star formation rate intensity distribution function $h(x)$ at values of the star formation rate intensity x down to the noise thresholds of the images. Finally, we *excluded* measurements of $h(x)$ at values of x less than the values that could have been detected at the 5σ level over 95% of the angular area of the survey. The segmentation maps that define the isophotal apertures of the galaxies contain, of course, pixels of insignificant or even negative measured energy flux (because the segmentation maps are defined with respect to smoothed versions of the images.) Thus low-intensity pixels near the edges of the segmentation maps are unsuitable for incorporation into the measurement of $h(x)$, since roughly half of these pixels have negative measured energy flux and so cannot bear on the analysis. Considering only high-intensity values of x eliminates the possibility that low-intensity pixels near the edges of the segmentation maps bias the measurement of $h(x)$. We verified that the measurement of $h(x)$ at our adopted star formation rate intensity thresholds is not affected by pixel-to-pixel noise by redetermining $h(x)$ from within the segmentation maps but with the actual images replaced by Gaussian noise (according to the actual noise properties of the images). The star formation rate intensity distribution function $h(x)$ is measured, say, in units of $\text{kpc}^2 (M_{\odot} \text{ yr}^{-1} \text{ kpc}^{-2})^{-1} \text{ Mpc}^{-3}$.

We determined measurement uncertainties of the star formation rate intensity distribution function $h(x)$ by applying a variation of the “bootstrap” resampling technique described previously by Lanzetta, Fernández-Soto, & Yahil (1998). The bootstrap resampling technique explicitly accounts for effects of sampling uncertainty, photometric uncertainty, and variance with respect to the spectrophotometric templates. First, we resampled objects from the catalogs (allowing the possibility of duplication), added random noise to the photometry (according to the actual noise properties of the images) and redetermined the photometric

redshift measurements, and added random noise to the photometric redshift measurements (according to the actual noise properties of the photometric redshift technique, as determined from the comparison of photometric and spectroscopic redshift measurements). Then, we determined the star formation rate intensity distribution function $h(x)$ from the resampled, perturbed catalogs of photometry and photometric redshifts exactly as from the actual catalogs of photometry and photometric redshifts. Finally, we repeated these steps a large number of times in order to trace out the distributions of measurement uncertainties.

7. RESULTS

Results of our analysis are shown in Figure 3, which plots the star formation rate intensity distribution function $h(x)$ versus the star formation rate intensity x as a function of redshift z . Several points are evident on the basis of Figure 3:

First, the star formation rate intensity threshold of the observations is a steep function of redshift, ranging from $x \approx 5 \times 10^{-4} M_{\odot} \text{ yr}^{-1} \text{ kpc}^{-2}$ at $z = 0.5$, to $\approx 0.3 M_{\odot} \text{ yr}^{-1} \text{ kpc}^{-2}$ at $z = 5$, to $\approx 1 M_{\odot} \text{ yr}^{-1} \text{ kpc}^{-2}$ at $z = 10$.

Second, at the redshifts $z \lesssim 1$ at which both low- and high-intensity star formation rate intensities can be measured, $\log h(x)$ versus $\log x$ is characterized by a relatively shallow dependence at $x \lesssim 10^{-2} M_{\odot} \text{ yr}^{-1} \text{ kpc}^{-2}$ and a relatively steep dependence at $x \gtrsim 10^{-2} M_{\odot} \text{ yr}^{-1} \text{ kpc}^{-2}$. The shallow dependence is sufficiently shallow and the steep dependence is sufficiently steep that, from equation (1), the bulk of the ultraviolet luminosity density is emitted where the two regions join, i.e. at $x \approx 10^{-2} M_{\odot} \text{ yr}^{-1} \text{ kpc}^{-2}$. This implies that to measure the bulk of the ultraviolet luminosity density requires sensitivity to star formation rate intensities *less than* the intensity $x \approx 10^{-2} M_{\odot} \text{ yr}^{-1} \text{ kpc}^{-2}$ at which $h(x)$ steepens. From Figure 3, it is clear that the observations of the Hubble Deep Fields—which are the most sensitive observations of faint galaxies ever obtained—can detect the intensities at which $h(x)$ steepens only to redshift $z \approx 1.5$ or at most $z \approx 2$; at higher redshifts, the observations are not sensitive to the intensities at which the bulk of the ultraviolet luminosity density are emitted.

Third, the high-intensity end of $h(x)$ —which is directly measured at all redshifts through $z \approx 10$ —evolves more or less monotonically toward higher values at higher redshifts. For example, at $x \approx 3 M_{\odot} \text{ yr}^{-1} \text{ kpc}^{-2}$, $h(x)$ evolves from $h(x) \approx 10^{-5} h_{100} \text{ kpc}^2 (M_{\odot} \text{ yr}^{-1} \text{ kpc}^{-2})^{-1} \text{ Mpc}^{-3}$ at $z \approx 1.5$ through $\approx 10^{-4} h_{100} \text{ kpc}^2 (M_{\odot} \text{ yr}^{-1} \text{ kpc}^{-2})^{-1} \text{ Mpc}^{-3}$ at $z \approx 2.5$ through $\approx 10^{-3} h_{100} \text{ kpc}^2 (M_{\odot} \text{ yr}^{-1} \text{ kpc}^{-2})^{-1} \text{ Mpc}^{-3}$ at $z \approx 4$. There are no local (say $z < 1$) analogs of the very high intensity (say $x > 1 M_{\odot} \text{ yr}^{-1} \text{ kpc}^{-2}$) regions that are seen

at higher redshifts, at least over the volumes probed by the Hubble Deep Fields.

To quantitatively establish the effect of the star formation rate intensity threshold of the observations on the determination of the star formation rate density, we fitted $h(x)$ versus x by a broken double power law model

$$h(x) = \begin{cases} A (x/x_0)^{-\alpha_1} & (x < x_0) \\ A (x/x_0)^{-\alpha_2} & (x \geq x_0), \end{cases} \quad (2)$$

which is described by slopes α_1 and α_2 at low and high intensities, characteristic intensity x_0 , and normalization A . First, we established fiducial parameters by fitting the model to the observations over the redshift interval $z = 0.5$ to 1. (These redshifts are low enough that the observations are sensitive to low values of x but not so low that redshift measurement uncertainties can significantly affect measurements of luminosity or star formation rate intensity.) Results indicate a low-intensity slope

$$\alpha_1 = -1.44_{-0.09}^{+0.22}, \quad (3)$$

a high-intensity slope

$$\alpha_2 = -3.05_{-0.33}^{+0.25}, \quad (4)$$

and a characteristic intensity

$$\log x_0 = -1.96 \pm 0.13 M_\odot \text{ yr kpc}^2. \quad (5)$$

The fiducial model is shown in Figure 3a. Next, we fitted simple variants of the fiducial model over other redshift intervals, fixing α_1 and α_2 and either (1) scaling vertically (i.e. fixing x_0 and varying A), (2) scaling horizontally (i.e. fixing A and varying x_0), and (3) scaling the break intensity [i.e. varying x_0 and A in such a way that $h(x)$ at low intensities does not change]. The variants of the fiducial model are shown in Figure 3b. Finally, we determined the star formation rate density versus redshift by integrating over the models, to intensities as low as the lowest star formation rate intensity $x = 6 \times 10^{-4} M_\odot \text{ yr}^{-1} \text{ kpc}^{-2}$ observed in the local universe (Kennicutt 1998).

Results are shown in Figure 4a, which plots the unobscured star formation rate densities versus redshift obtained by integrating over the models. For comparison, Figure 4a also plots the unobscured star formation rate density versus redshift obtained by Madau et al. (1996, 1998) by summing over the observed galaxy energy fluxes. From Figure 4a, it is evident that the ultraviolet luminosity density obtained by integrating over the models increases more or less monotonically with redshift, for each of the three models. Over the redshift interval $z = 0$ through 10, the increase ranges from a factor 10 (for scaling the break intensity of the fiducial model) through a factor 250 (for scaling the fiducial model vertically). The

ultraviolet luminosity density obtained by Madau et al. (1996, 1998) by summing over the observed galaxy energy fluxes significantly underestimates the unobscured star formation rate density obtained by integrating over the models at redshifts larger than $z \approx 2$. The increase of the ultraviolet luminosity density with redshift is a direct consequence of the monotonic increase of the incidence of the highest intensity star forming regions with redshift and must hold unless the actual functional form of $h(x)$ at redshifts $z \gtrsim 2$ differs dramatically from the functional forms of the three simple variants of the fiducial model. We conclude that the unobscured star formation rate density—or equivalently the ultraviolet luminosity density—plausibly increases monotonically with redshift through the highest redshifts observed.

But it also appears from Figure 4a that our measurements and the measurements of Madau et al. (1996, 1998) of the unobscured star formation rate density are discordant at redshifts $z = 0$ to 2. This is a consequence not of cosmological surface brightness dimming effects but rather of a mismatch of the rest-frame wavelengths from which the star formation rate densities were measured. We measured star formation rate densities by scaling from measured luminosity densities at rest-frame wavelength 1500 Å at all redshifts. In contrast, Madau et al. (1996, 1998) measured star formation rate densities by scaling from measured luminosity densities at rest-frame wavelength 2800 Å at redshifts $z < 2$ (based on results of Lilly et al. 1996 and Connolly et al. 1997) and at rest-frame wavelength 1500 Å at redshifts $z > 2$ (based on results from the Hubble Deep Field), adopting a *flat* f_ν spectrum to scale luminosity density to star formation rate density. Thus our measurements and the measurements of Madau et al. (1996, 1998) should be consistent only if the rest-frame ultraviolet luminosity density of the universe exhibits a flat f_ν spectrum at redshifts $z = 0$ to 2.

To test this possibility, we measured the spectrum of the luminosity density versus redshift, based on galaxies observed in the HDF and HDF-S using our catalog of photometry and photometric redshifts. Results are shown in Figure 5. The ratio of the luminosity density at rest-frame wavelength 2800 Å to the luminosity density at rest-frame wavelength 1500 Å is ≈ 2 at redshifts $z < 2$. In other words, the flat f_ν spectrum adopted by Madau et al. (1996, 1998) is *inconsistent* with the measured spectrum of the luminosity density at redshifts $z < 2$. Consequently, the measurements of Madau et al. (1996, 1998) at redshifts $z < 2$ must be *reduced* by a factor ≈ 2 to bring them into consistency with measurements of the star formation rate density based on rest-frame 1500 Å luminosity density. The results corrected in this way are shown in Figure 4b. It appears from Figure 4b that our measurements and the corrected measurements of Madau et al. (1996, 1998) of the unobscured star formation rate density are consistent at redshifts $z < 2$.

Adoption of the currently favored non-zero cosmological constant cosmological model of vacuum energy density $\Omega_\Lambda = 0.7$ and matter density $\Omega_M = 0.3$ does not qualitatively

change our conclusions. Under this cosmological model, the values of the unobscured star formation densities are reduced, by amounts that range from $\approx 20\%$ for the lowest-redshift point to $\approx 50\%$ for the highest-redshift point.

8. CONNECTION WITH THE NEUTRAL HYDROGEN COLUMN DENSITY DISTRIBUTION FUNCTION

The star formation rate intensity distribution function $h(x)$ is exactly analogous to the column density distribution function $f(N)$ (as a function of neutral hydrogen column density N) measured from damped Ly α absorption systems detected toward high-redshift background QSOs in that $h(x)dx$ and $f(N)dN$ both measure incidence per length of cosmologically distributed material. The connection between $h(x)$ and $f(N)$ can be made explicit by adopting a “Kennicutt” (1998) relation between star formation rate intensity x and neutral hydrogen column density N

$$x = 8.9 \times 10^{-5} \left(\frac{N}{1.2 \times 10^{20} \text{ cm}^{-2}} \right)^{1.4} M_{\odot} \text{ yr}^{-1} \text{ kpc}^{-2}. \quad (6)$$

(Kennicutt 1998 multiplied observed energy fluxes by a factor 2.8 to correct for effects of obscuration by intervening dust. Here we divide the energy fluxes of Kennicutt 1998 by this factor 2.8 to *uncorrect* for effects of obscuration by intervening dust, i.e. to establish a relation between *unobscured* star formation rate intensity x and gas column density N . We consider neutral hydrogen column density to represent gas column density because the molecular content of high column density QSO absorption systems is measured to be low.) Then $h(x)$ and $f(N)$ are related as

$$h(x) dx dl = f(N) dN dX, \quad (7)$$

where dl is a comoving length element and dX is an absorption distance element. We applied equations (6) and (7) to express measurements of $f(N)$ at redshifts $z \approx 1.6$ through 5 (Lanzetta et al. 1991; Storrie-Lombardi, Irwin, & McMahon 1996) in terms of $h(x)$.

Results are shown in Figure 3b. The amplitude of the measurements of $f(N)$ at redshifts $z \approx 1.6$ through 5 expressed in terms of $h(x)$ match the amplitude of the measurements of $h(x)$. Further, application of equation (5) to a power-law form of the column density distribution function $f(N) \propto N^{-\beta}$ of slope $\beta = 1.48 \pm 0.30$ (Storrie-Lombardi, Irwin, & McMahon 1996) predicts a power-law form of the star formation rate intensity distribution function $h(x) \propto x^{-\alpha_1}$ of slope $\alpha_1 = 1.34 \pm 0.22$, which is in excellent agreement with the slope $\alpha_1 = 1.44_{-0.09}^{+0.22}$ measured at redshifts $z = 0.5$ to 1. We take the remarkable agreement

between $f(N)$ expressed in terms of $h(x)$ and $h(x)$ —in terms of both amplitude and slope—to (1) suggest that the actual functional form of $h(x)$ at redshifts $z \gtrsim 2$ does not differ dramatically from the function forms of the three simple variants of the fiducial model (and that the third variant is slightly favored over the other two variants) and (2) establish a quantitative connection between high-redshift galaxies and high column density gas and suggest that high-redshift damped Ly α absorption systems trace lower star formation rate intensity regions of the same galaxies detected in star light in the HDF and HDF–S.

Of course, $f(N)$ and $h(x)$ are measured on very different physical scales. Specifically, $f(N)$ is measured on a physical scale of ≈ 1 pc (which is set by the size of the continuum emitting regions of QSOs), whereas $h(x)$ is measured on a physical scale of ≈ 200 pc (which is set by the angular resolution of the HDF and HDF–S images). The remarkable agreement between $f(N)$ expressed in terms of $h(x)$ and $h(x)$ nevertheless establishes that faint galaxies in the HDF and HDF–S obey a *statistical* Kennicutt (1998) relation that is consistent with the Kennicutt (1998) relation of nearby galaxies. In other words, the relationship between column density measured on a scale of ≈ 1 pc and star formation rate intensity measured on a scale of ≈ 200 pc for faint galaxies in the HDF and HDF–S is *on average* consistent with the relationship between column density and star formation rate intensity measured on galactic scales for nearby galaxies.

9. SUMMARY AND CONCLUSIONS

We address the effects of cosmological surface brightness dimming on observations of faint galaxies by examining the distribution of “unobscured” star formation rate intensities versus redshift, which we use to assess the ultraviolet luminosity density versus redshift, using our photometry and photometric redshift measurements of faint galaxies in the HDF and the HDF–S WFPC2 and NICMOS fields. We find the following results:

1. Previous measurements have missed a dominant fraction of the ultraviolet luminosity density of the universe at high redshifts by neglecting cosmological surface brightness dimming effects, which are important at redshifts larger than $z \approx 2$.
2. The incidence of the highest intensity star forming regions increases monotonically with redshift.
3. The ultraviolet luminosity density plausibly increases monotonically with redshift through the highest redshifts observed.
4. Previous measurements of the ultraviolet luminosity density at redshifts $z < 2$ must

be reduced by a factor ≈ 2 to allow for the spectrum of the luminosity density between rest-frame wavelengths 1500 and 2800 Å.

5. The distribution of star formation rate intensities matches the distribution of neutral hydrogen column densities at redshifts $z \approx 2$ through 5, which establishes a quantitative connection between high-redshift galaxies and high column density gas and suggests that high-redshift damped Ly α absorption systems trace lower star formation rate intensity regions of the same galaxies detected in star light in the HDF and HDF-S.

Because our measurements neglect the effects of obscuration by dust, they represent *lower limits* to the total star formation rate density. Our analysis suggest that star formation in the very early universe may have occurred at a much higher rate than is generally believed and that cosmological surface brightness dimming effects cannot be ignored when interpreting statistical properties of the high-redshift galaxy population.

This research was supported by NASA grant NAGW-4422 and NSF grant AST-9624216. AFS was supported by a European Union Marie Curie Fellowship. The authors acknowledge helpful comments from an anonymous referee.

TABLE 1
DETAILS OF THE OBSERVATIONS

Field	Bandpass	Reference
HDF	F300W	1
	F450W	1
	F606W	1
	F814W	1,2
	F110W	3,4
	F160W	3,4
	<i>J</i>	5
	<i>H</i>	5
	<i>K</i>	5
	HDF–S WFPC2	F300W
F450W		6
F606W		6
F814W		6
<i>U</i>		7
<i>B</i>		7
<i>V</i>		7
<i>R</i>		7
<i>I</i>		7
<i>J</i>		7
<i>H</i>		7
<i>K</i>		7
HDF–S NICMOS		F110W
	F160W	8
	F222M	8
	<i>U</i>	9
	<i>B</i>	9
	<i>V</i>	9
	<i>R</i>	9
	<i>I</i>	9

REFERENCES—(1) Williams et al. (1996); (2) Gilliland, Nugent, & Phillips (1999); (3) Thompson et al. (1999); (4) Dickinson et al. (2000); (5) Dickinson et al. (2001), in preparation; (6) Casertano et al. (2000); (7) da Costa et al. (2001); (8) Williams et al. (2000); (9) ESO VLT–UT1 Science Verification (1998).

TABLE 2
DETAILS OF THE OBJECT DETECTION

Field	Object Detection Bandpasses
HDF	F814W, F160W, <i>K</i>
HDF-S WFPC2	F814W, <i>H</i> , <i>K</i>
HDF-S NICMOS	F160W, F222M

REFERENCES

- Bertin, E., & Arnouts, S. 1996, *A&AS*, 117, 393
- Casertano, S., et al. 2000, *AJ*, 120, 2747
- Connolly, A. J., Szalay, A. S., Dickinson, M., Subbarao, M. U., & Brunner, R. J. 1997, *ApJ*, 486, L11
- da Costa, L., et al. 1998, *A&A*, submitted
- Dickinson, M., et al. 2000, *ApJ*, 531, 624
- Fernández-Soto, A., Lanzetta, K. M., & Yahil, A. 1999, *ApJ*, 513, 34
- Fernández-Soto, A., Lanzetta, K. M., Chen, H.-W., Pascarelle, S., & Yahata, N. 2001, *ApJS*, in press
- Gilliland, R. L., Nugent, P. E., & Phillips, M. M. 1999, *ApJ*, 521, 30
- Hopkins, A. M., Connolly, A. J., & Szalay, A. S. 2000, *AJ*, 2843
- Kennicutt, R. C. Jr. 1998, *ApJ*, 498, 541
- Lanzetta, K. M., Fernández-Soto, A., & Yahil, A. 1998, in *The Hubble Deep Field, proceedings of the Space Telescope Science Institute 1997 May Symposium*, eds. M. Livio, S. M. Fall, & P. Madau (Cambridge University Press: Cambridge), p. 143
- Lanzetta, K. M., Wolfe, A. M., Turnshek, D. A., Lu, L., McMahon, R. G., & Hazard, C. 1991, *ApJS*, 77, 1
- Lanzetta, K. M., Yahil, A., & Fernández-Soto, A. 1996, *Nature*, 381, 759
- Lilly, S. J., Le Fevre, O., Hammer, F., & Crampton, D. 1996, *ApJ*, 460, L1
- Madau, P., Ferguson, H. C., Dickinson, M. E., Giavalisco, M., Steidel, C. C., & Fruchter, A. 1996, *MNRAS*, 283, 1388
- Madau, P., Pozzetti, L., & Dickinson, M. 1998, *ApJ*, 498, 106
- Pascarelle, S. M., Lanzetta, K. M., & Fernández-Soto, A. 1998, *ApJ*, 508, L1
- Puetter, R. C., & Yahil, A. 1999, in *ASP Conf. Ser. Vol. 172, Astronomical Data Analysis Software and Systems VIII*, eds. D. M. Mehringer, R. L. Plante & D. A. Roberts (ASP: San Francisco), p. 307
- Somerville, R. S., Primack, J. R., & Faber, S. M. 2001, *MNRAS*, 320, 504
- Steidel, C. C., Adelberger, K. L., Giavalisco, M., Dickinson, M., & Pettini, M. 1999, *ApJ*, 519, 1
- Storrie-Lombardi, L. J., Irwin, M. J., & McMahon, R. G. 1996, *MNRAS*, 282, 1330

- Thompson, R. I., Storrie-Lombardi, L. J., Weymann, R. J., Rieke, M. J., Schneider, G., Stobie, E., Lytle, D. 1999, *AJ*, 117, 17
- Williams, R. E., et al. 1996, *AJ*, 112, 1335
- Williams, R. E., et al. 2000, *AJ*, 120, 2735
- Yahata, N., Lanzetta, K. M., Chen, H.-W., Fernández-Soto, A., Pascarelle, S., Yahil, A., & Puetter, R. C. 2000, *ApJ*, 538, 493

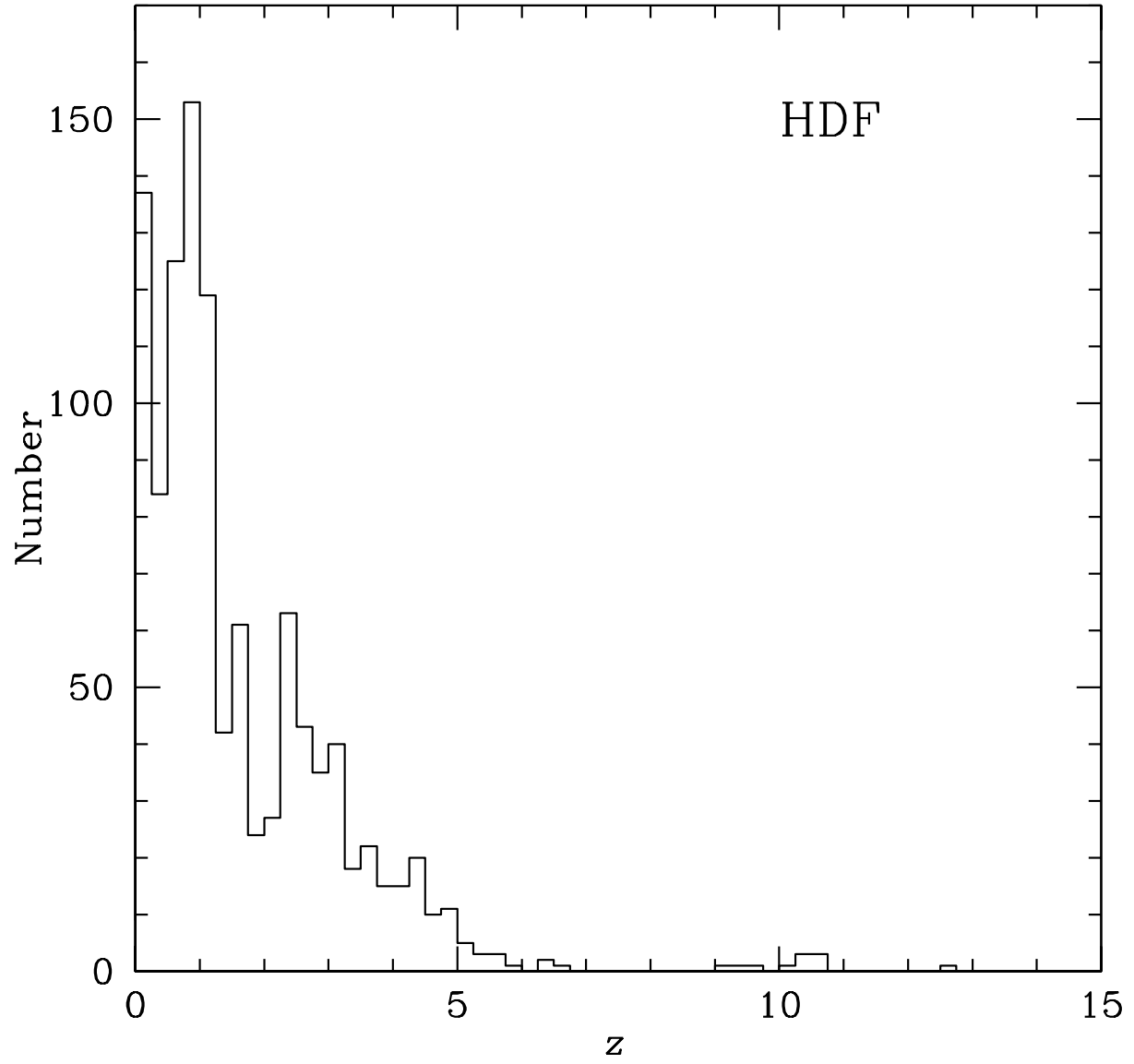
Fig. 1.— Angular area Ω accessible to the observations as a function of logarithm of star formation rate intensity x and redshift z . Star formation rate intensity x is measured in units of $M_{\odot} \text{ yr}^{-1} \text{ kpc}^{-2}$. White represents $\Omega = 0$, black represents $\Omega = 11.7 \text{ arcmin}^2$, and grey represents intermediate values of Ω .

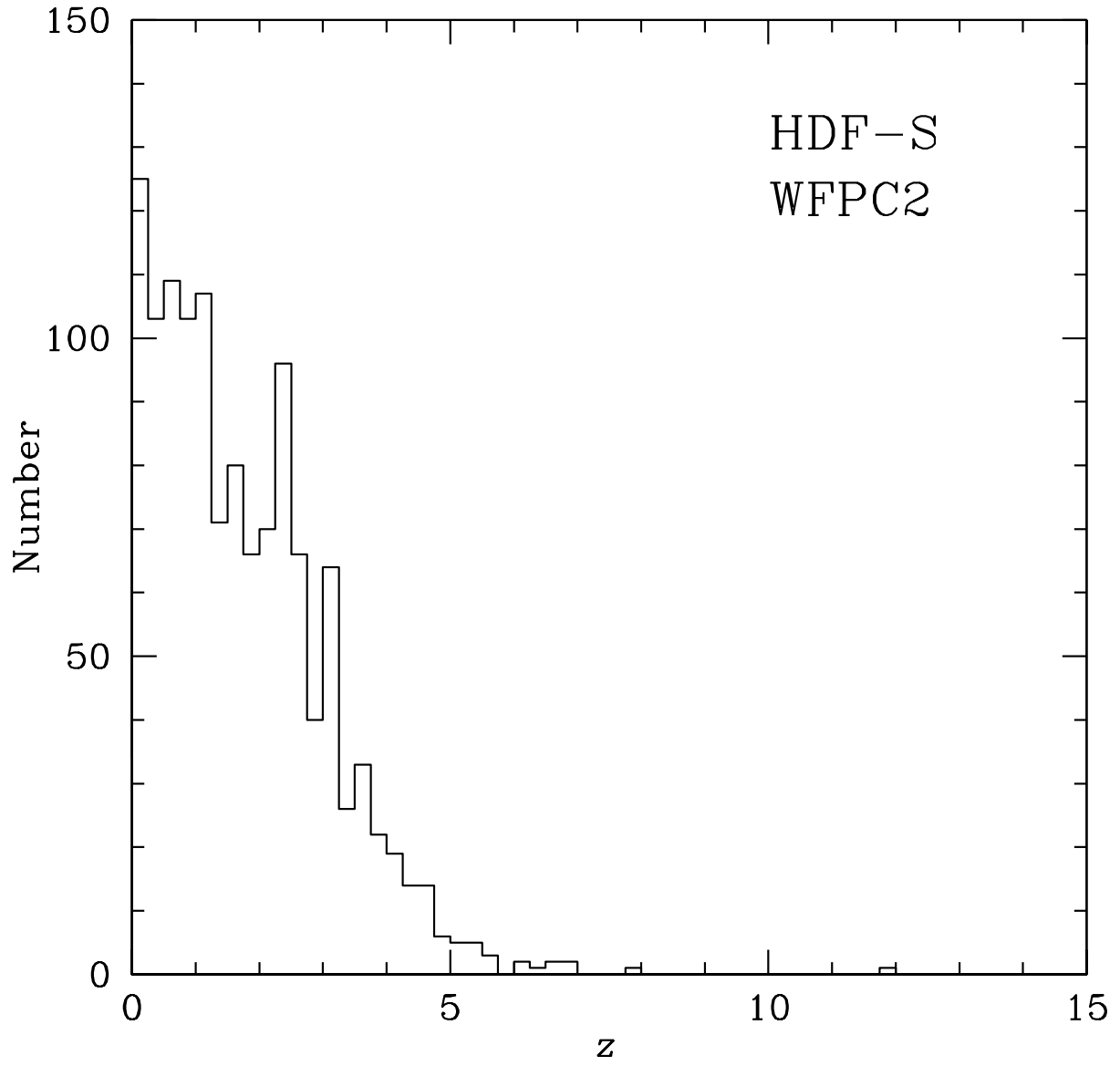
Fig. 2.— Redshift measurement distributions of all galaxies identified in the (a) HDF and HDF-S (b) WFPC2 and (c) NICMOS fields.

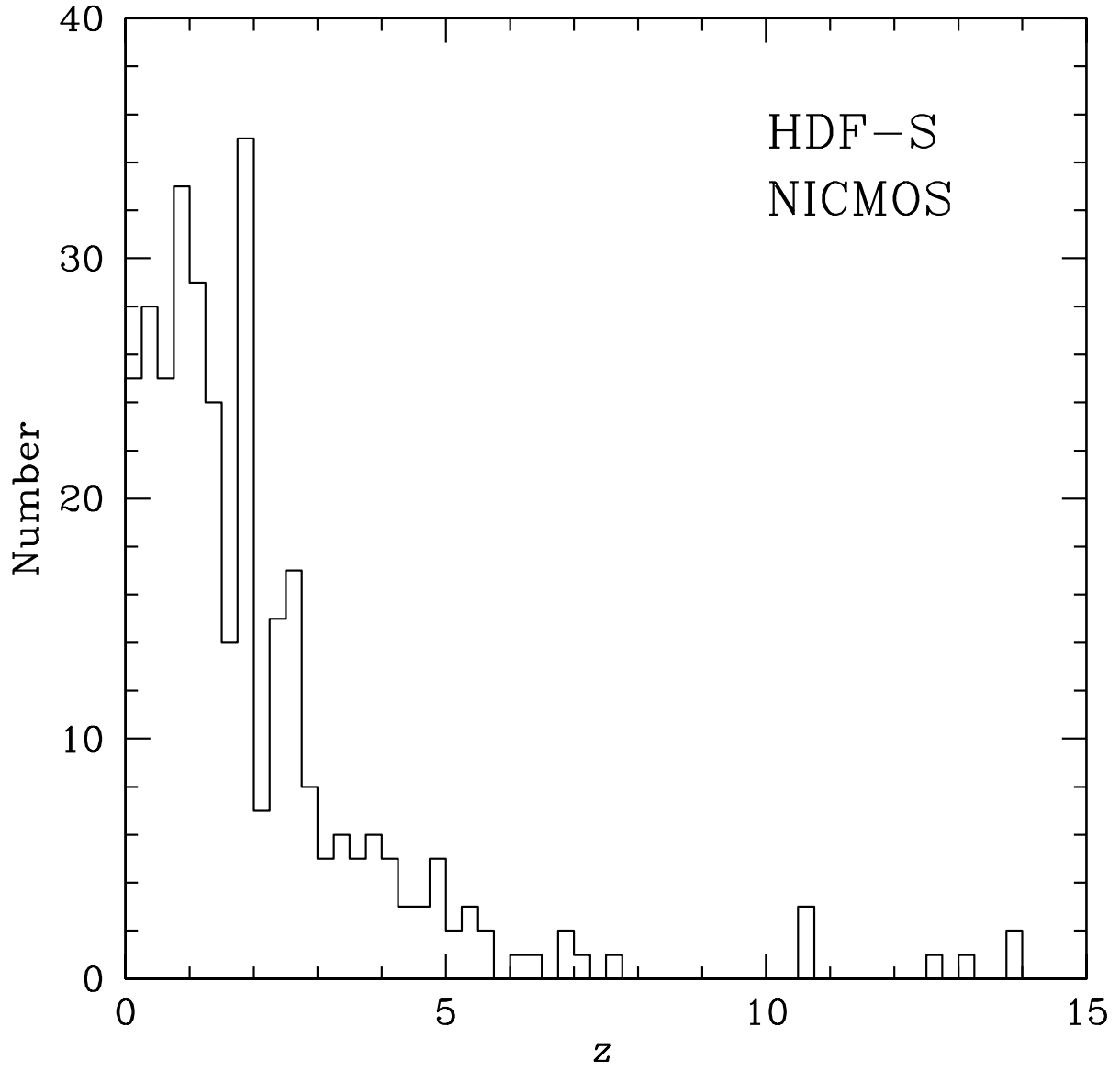
Fig. 3.— Star formation rate intensity distribution function $h(x)$ versus star formation rate intensity x at redshifts ranging from $z = 0$ to 0.5 through $z = 6$ to 10. Vertical error bars show 1σ uncertainties (determined by a bootstrap resampling technique), and horizontal error bars show bin sizes. (For many points, the vertical error bars are smaller than the points.) (a) Black circles show $h(x)$ determined from observations of faint galaxies. Green line segments show the best-fit broken double power law model fitted to the observations at redshifts $z = 0.5$ to 1. (b) Black circles show $h(x)$ determined from observations of faint galaxies. Magenta open circles show $h(x)$ determined by expressing measurements of $f(N)$ in terms of $h(x)$. Line segments show variants of the best-fit broken double power law model obtained by scaling vertically (red), scaling horizontally (blue), and scaling the break intensity (green).

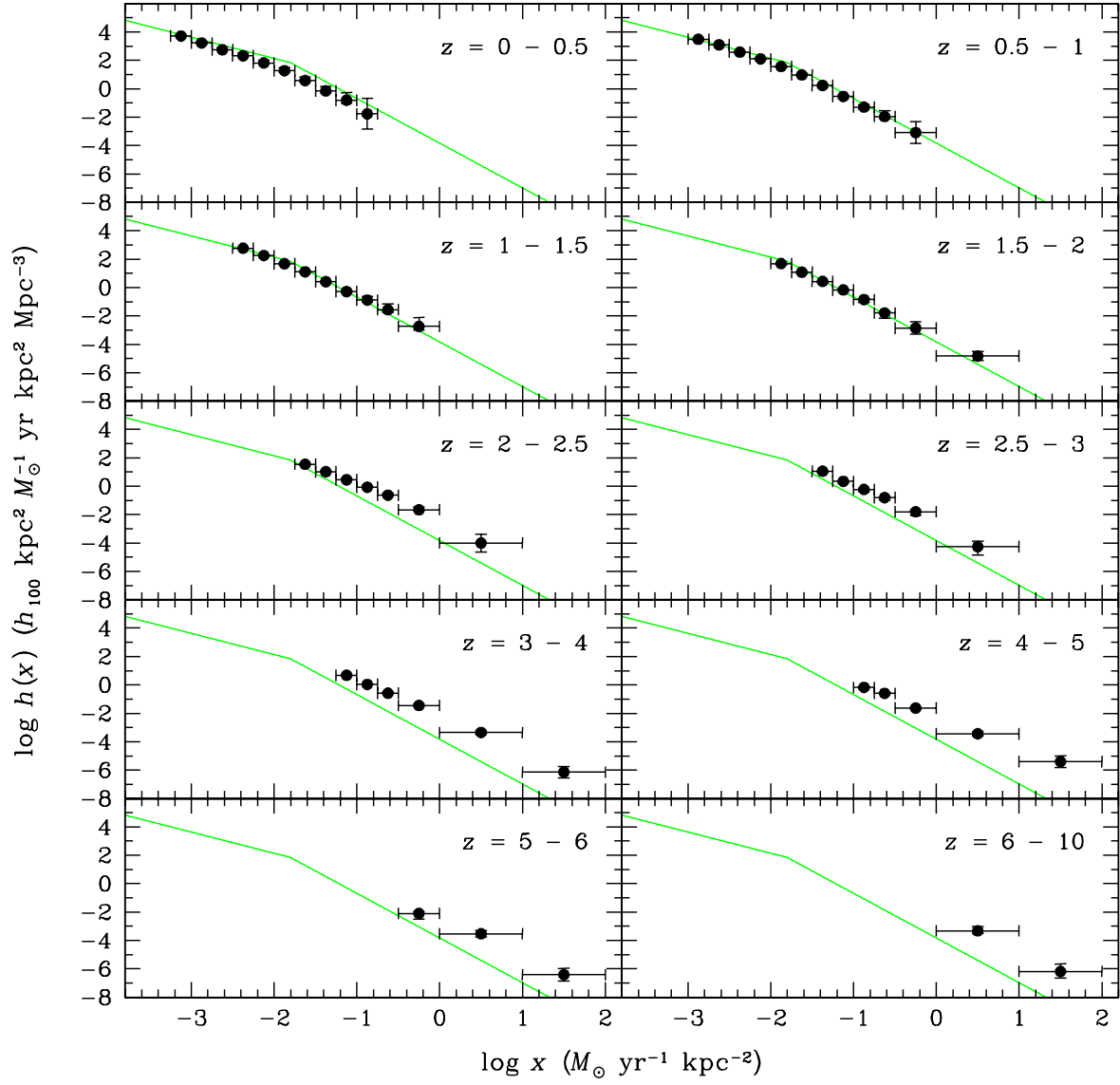
Fig. 4.— (a) Unobscured star formation rate densities $\dot{\rho}_S$ versus redshift z . Points plot unobscured star formation rate densities versus redshift obtained by integrating over the models, fixing α_1 and α_2 and either (1) scaling vertically (red squares), (2) scaling horizontally (blue triangles), and (3) scaling the break intensity (green circles) and the unobscured star formation rate density versus redshift obtained by Madau et al. (1996, 1998) by summing over the observed galaxy energy fluxes (black open circles). Vertical error bars show 1σ uncertainties, which for the red squares, blue triangles, and green circles are determined by a bootstrap resampling technique. (b) Same as (a), except that the measurements of Madau et al. (1996, 1998) at redshifts $z < 2$ are reduced by a factor 2 to bring them into consistency with measurements of the star formation rate density based on rest-frame 1500 Å luminosity density.

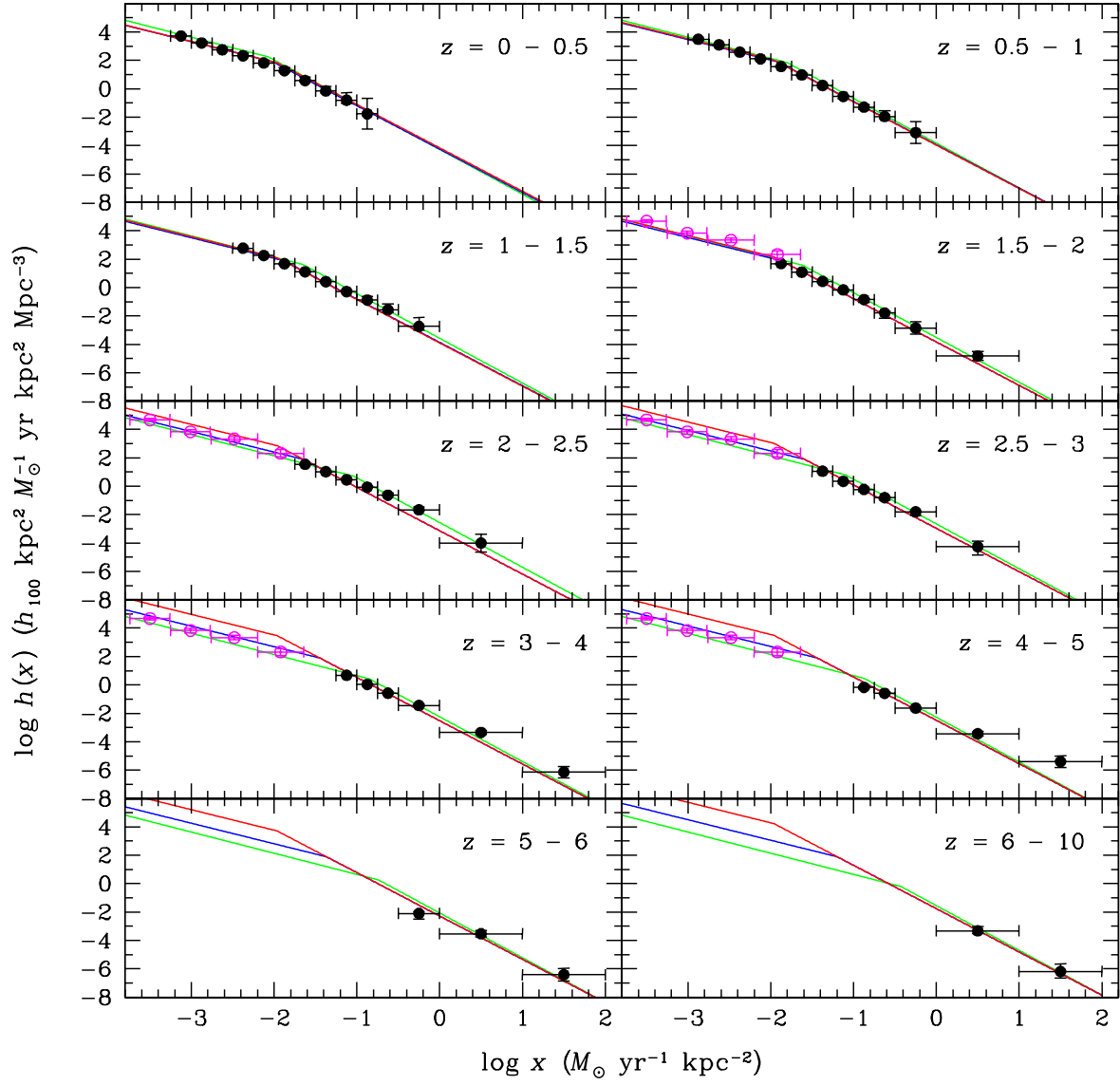
Fig. 5.— Ratio of the luminosity density at rest-frame wavelength 2800 Å to the luminosity density at rest-frame wavelength 1500 Å at redshifts $z < 10$, based on galaxies observed in the HDF and HDF-S using our catalog of photometry and photometric redshifts.

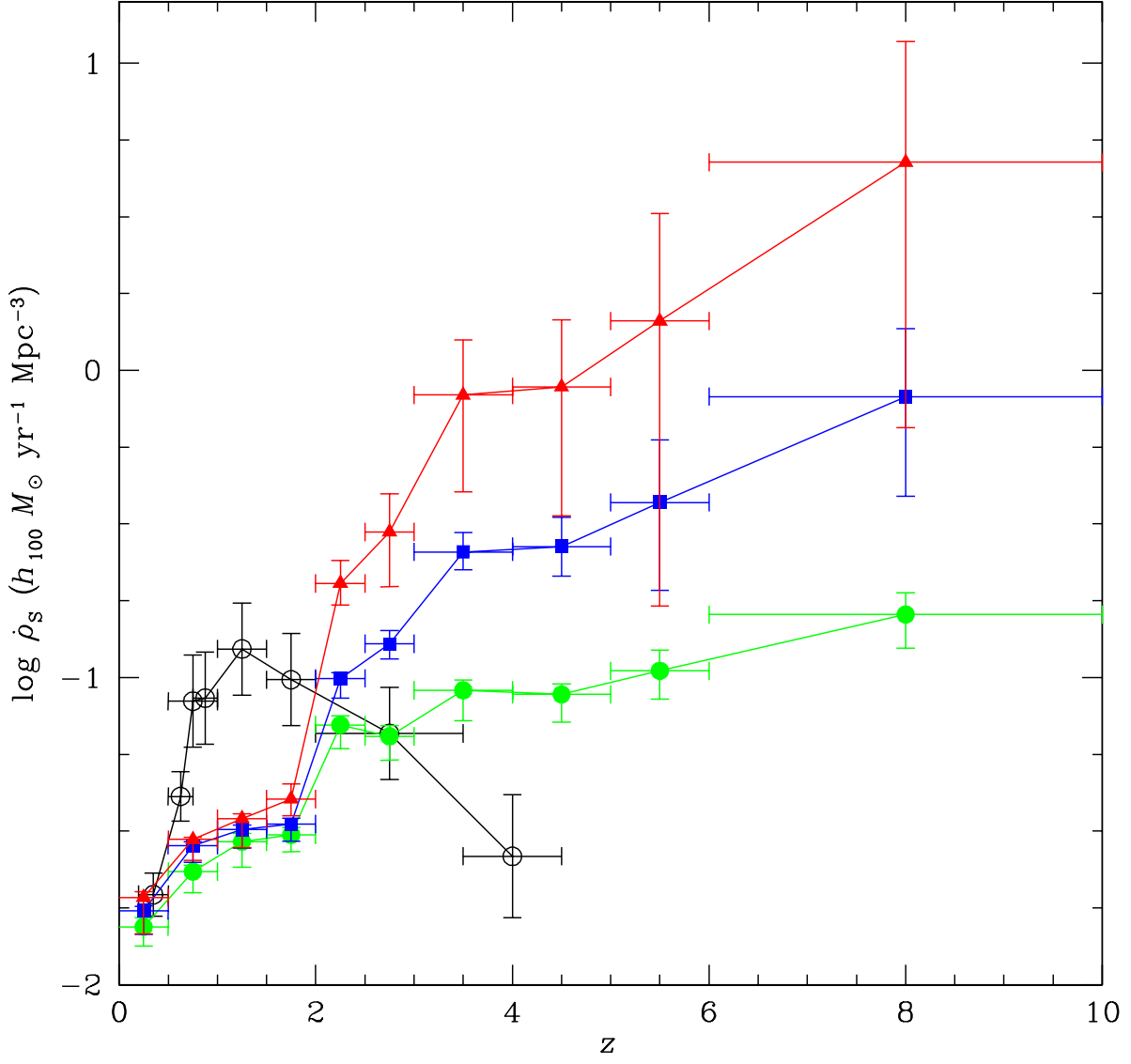


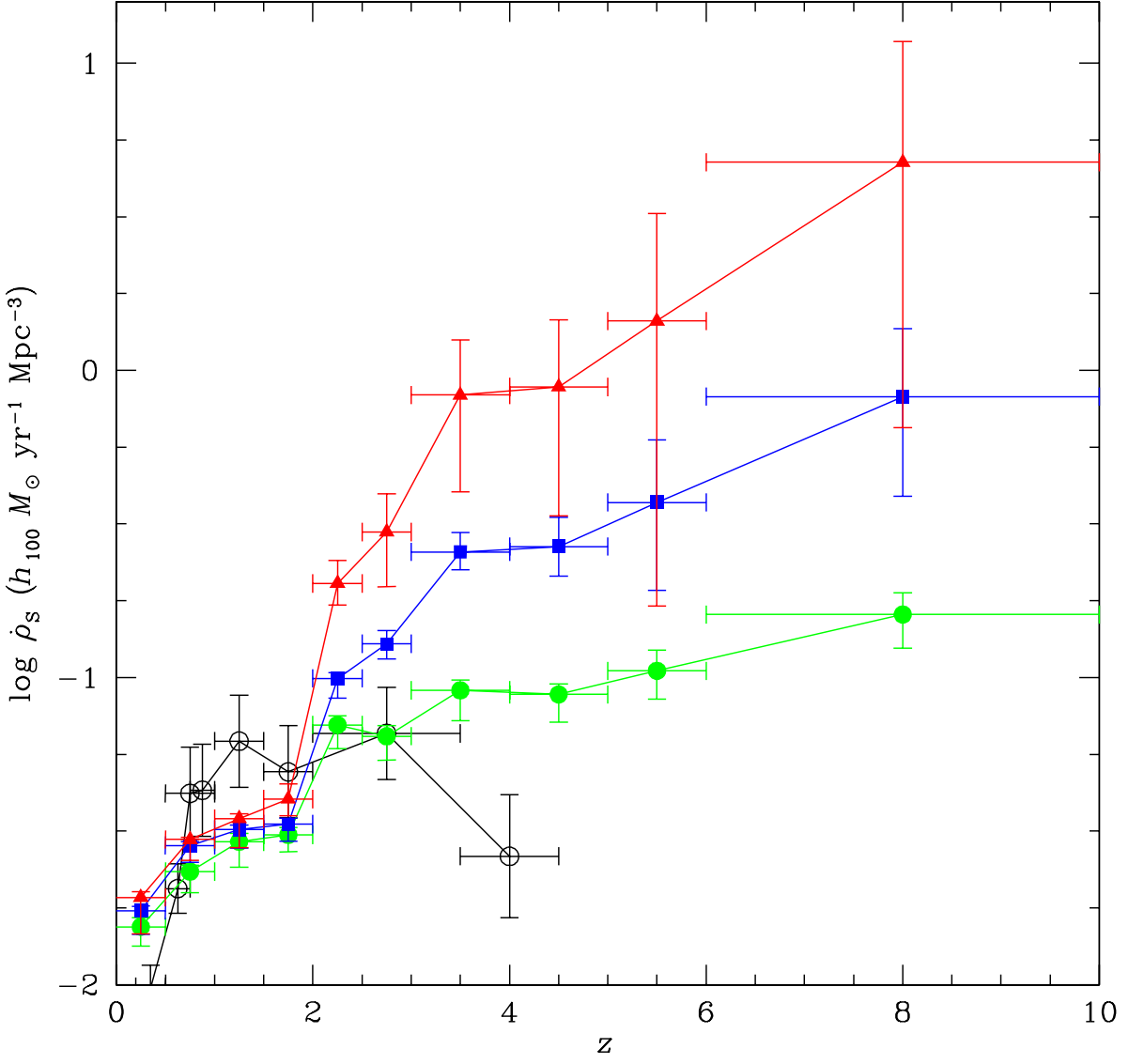


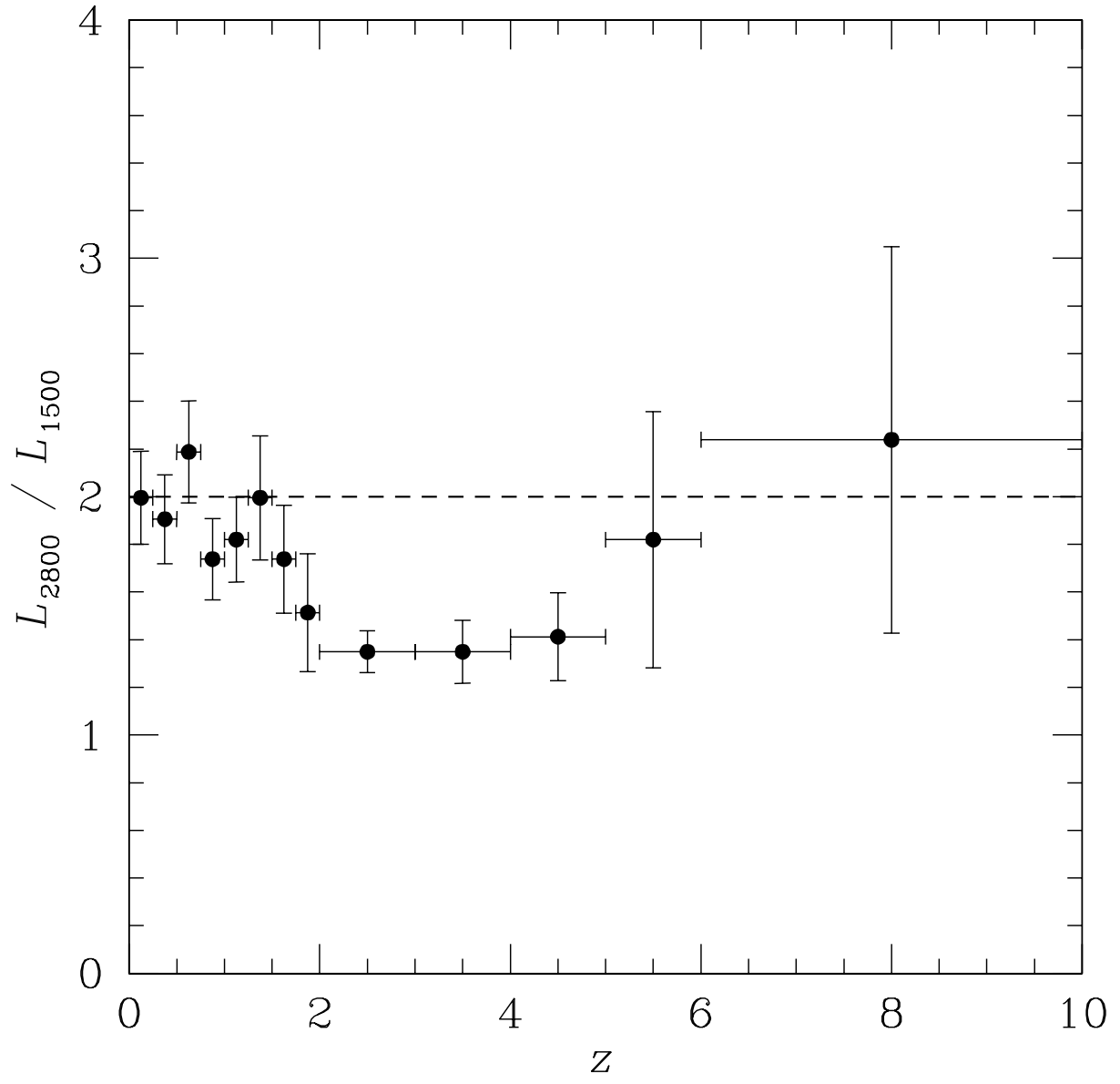












This figure "f1.gif" is available in "gif" format from:

<http://arxiv.org/ps/astro-ph/011129v1>